

View Article Online **PAPER**

cementing suspensions†



Cite this: Soft Matter, 2020, **16**, 3929

> Iman Mehdipour, Da Hakan Atahan, ab Narayanan Neithalath, Mathieu Bauchy, de Edward Garboczif and Gaurav Sant*aegh

How clay particulates affect flow cessation and

the coiling stability of yield stress-matched

The remarkable increase in the flow resistance of dense suspensions can hinder 3D-printing processes on account of flow cessation in the extruder, and filament fragility/rupture following deposition. Understanding the nature of rheological changes that occur is critical to manipulate flow conditions or to dose flow modifiers for 3D-printing. Therefore, this paper elucidates the influences of clay particulates on controlling flow cessation and the shape stability of dense cementing suspensions that typically feature poor printability. A rope coiling method was implemented with varying stand-off distances to probe the buckling stability and tendency to fracture of dense suspensions that undergo stretching and bending during deposition. The contributions of flocculation and short-term percolation due to the kinetics of structure formation to deformation rate were deconvoluted using a stepped isostress method. It is shown that the shear stress indicates a divergence with a power-law scaling when the particle volume fraction approaches the jamming limit; $\phi o \phi_{\rm i} pprox \phi_{\rm max}$. Such a power-law divergence of the shear stress decreases by a factor of 10 with increasing clay dosage. Such behavior in clay-containing suspensions arises from a decrease in the relative packing fraction (ϕ/ϕ_{max}) and the formation of fractally-architected aggregates with stronger interparticle interactions, whose uniform arrangement controls flow cessation in the extruder and suspension homogeneity, thereby imparting greater buckling stability. The outcomes offer new insights for assessing/improving the extrudability and printability behavior during slurry-based 3D-printing process.

Received 7th December 2019 Accepted 25th March 2020

DOI: 10.1039/c9sm02414j

rsc li/soft-matter-journal

1. Introduction and background

To create materials that are amenable to 3D-printing, it is advantageous to combine powder feedstocks with a carrier liquid (often water) to form a concentrated suspension ("slurry"). 1,2 The suspension can then be printed layer-by-layer (i.e., in the form of a filament) by extrusion through a printer nozzle assisted by air-pressure, a ram or screw auger.2-4 It is broadly accepted that suspensions amenable to layer-wise extrusion/deposition 3D-printing can be composed by adjusting the rheological properties of the suspension.⁵⁻⁹ Suspensions with suitable rheological properties feature the ability: (i) to be extruded through a print nozzle without experiencing flow cessation, 10-12 (ii) to support the weight of the printed layer itself, and of overlying layers, 9,13 and (iii) to be shape stable while limiting the potential for filament rupture during extrusion/deposition. 12,14 In 3D-printing of suspensions, two competing failure modes are typically noted: (i) material failure by yielding, and (ii) elastic buckling failure through local or global instability, which in turn may be accompanied by material failure. 15,16 The failure mode depends on the printed object's geometry, the kinetics of (the suspension's) structure formation,

^a Laboratory for the Chemistry of Construction Materials (LC²), Department of Civil and Environmental Engineering, University of California, Los Angeles, CA 90095, USA. E-mail: gsant@ucla.edu; Tel: +1-310 206-3084

^b Department of Civil Engineering, Istanbul Technical University, Istanbul, Turkey ^c School of Sustainable Engineering and the Built Environment, Arizona State University, Tempe, AZ, USA

^d Laboratory for the Physics of Amorphous and Inorganic Solids (PARISlab), Department of Civil and Environmental Engineering, University of California, Los Angeles, CA 90095, USA

^e Institute for Carbon Management (ICM), University of California, Los Angeles,

f Applied Chemicals and Materials Division, Material Measurement Laboratory. National Institute of Standards and Technology, Boulder, CO 80305, USA

g Department of Materials Science and Engineering, University of California, Los Angeles, CA 90095, USA

^h California Nanosystems Institute (CNSI), University of California, Los Angeles, CA 90095, USA

[†] Electronic supplementary information (ESI) available: Coiling speed with air pressure, kinetics of structure formation at varying rest times, dynamic light scattering of flocs, rheological properties with particle volume fraction, interparticle interaction potential between clay particles, rheological hysteresis, shear thickening/thinning behavior, strain-retardation time, and viscoelastic properties, See DOI: 10.1039/c9sm02414i

i.e., post-extrusion/-deposition, the shear history of the suspension prior to extrusion, 17-19 loading rate, boundary conditions, and process parameters (e.g., print speed, nozzle distance). 12,20

To ensure shape stability during the 3D-printing process, particulate suspensions are often composed at a high solid volume fraction ($\phi \geq 0.40$). 9,21,22 Such dense particulate suspensions generally display non-Newtonian flow behaviors, including shear thinning, shear thickening, and shear-induced jamming. 23-26 Shear jamming, where flow is arrested and the suspension exhibits solid-like behavior, is understood to be strongly dominated by particle volume fraction and interparticle interactions.^{27–31} To approach the shear jamming regime, both a minimum stress level (or, equivalently, a minimum shear rate) and a sufficiently high packing fraction ($\phi \rightarrow \phi_i$) are required.³⁰ Dense suspensions exhibit high shear rate dependence: at low applied shear, most particles in the suspension are lubricated by solvent layers, thus shear thinning is observed, whereas at high shear, a large fraction of particles are forced into close proximity, such that the lubrication layer can rupture or is reduced to molecular length-scales, resulting in shear thickening behavior. 25,26,32-34 As a result, particles make direct (Hertzian) contacts and experience friction. This effect becomes more critical as ϕ approaches $\phi_{\rm max}$ where $\phi_{\rm max}$ ranges between 0.50 to 0.60, which can lead to flow cessation and shear-induced iamming.33,35-37 This behavior can cause heterogeneity in the arrangement of neighboring particles and fragility; in dense suspensions when subjected to shear. 36,38,39 For instance, the consolidation of dense suspensions during 3D-printing has been observed to result in differing (spatial) solid concentrations as a function of position due to liquid phase migration. 10,11,39 Such increases in solid concentration due to liquid phase migration can cause the suspension's transition from flowing to solid-like state, thereby resulting in flow cessation in the extruder. Although the complexity of the rheological behavior of dense suspensions has been extensively studied, it remains unclear how such attributes impact printability and filament homogeneity during the 3D-printing processes.

The kinetics of structure formation in a dense cementitious suspension are critical for 3D-printing. This requires, in general, that the time-dependent evolution of the yield stress of suspension should be sufficient to prevent the flow of the printed layer itself, and the ability to resist force amplification associated with the deposition of overlying layers (see Fig. 1a). Furthermore, the rate and extent of structure formation also control the rate and extent of deformation of the printed layer, i.e., both at short and later times (see Fig. 1b). For example, while thixotropic rebuilding associated with flocculation is relevant at short time scales, rigid structure formation associated with the progress of hydration reactions dominates at later times. 13,40 While structure formation is necessary and important, it needs to be controlled, since it can induce issues such as: (i) flow cessation during extrusion, (ii) filament rupture during deposition, and (iii) poor interface bonding between layers after deposition. To affect such structure

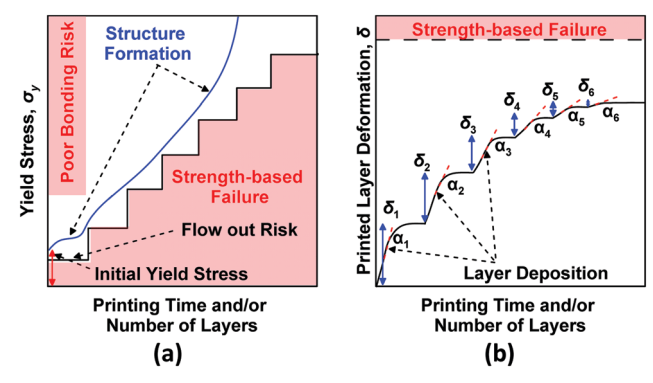


Fig. 1 Representative schematic that illustrates: (a) time-dependent yield stress evolution of a printed layer that is required to prevent the flow of the layer itself after extrusion as well as its ability to support subsequent overlying layers, and (b) reduced deformation of the deposited layer due to its structure build-up following deposition of subsequent overlying layers. Here, α and δ refer to the rate and extent of deformation of the printed layer, respectively, following the deposition of subsequent layers. In (a), the interface bonding between layers is controlled by the yield stress of the layer immediately after deposition. If the yield stress of a printed layer is much greater than the minimum required to support itself, it can result in poorly-bonded interfaces between successive layers due to the lack of local remixing/homogenization and formation of high local porosity.51

formation rates, colloidal particles such as clays have been added to cementitious suspensions. Clay particulates feature a platelike morphology consisting of negatively charged faces and positively charged edges. 41-43 This anisotropic surface charge results in the formation of the house of cards-like structures within the suspension. 44-46 Therefore, clay suspensions feature high thixotropic rebuilding rates (i.e., recovery rate)^{47,48} and stretchability,^{49,50} which leads to superior shape stability while minimizing the risk of filament rupture during printing. This enables accelerated printing and allows flexibility in the stand-off distance (i.e., distance from the print nozzle tip to substrate) and print path curvature.

Although the role of clay additions on improving suspension printability is well-known, the means by which clay particulates mitigate flow cessation and enhance the homogeneity of suspension during extrusion is less well-understood. To better address these questions, this paper seeks to develop new insights into how clay incorporation affects flow cessation in extruder and suspension homogeneity during extrusion and its resulting shape stability following accelerated 3D-printing. Towards this end, a viscoelastic rope coiling approach (i.e., the examination of the coiling and falling of a viscoelastic rope onto a surface)52,53 is used to assess the buckling stability of a suspension that experiences stretching and bending during deposition. Taken together, the outcomes of this work help in the development of new guidelines for improving the printability and filament homogeneity of dense suspensions.

2. Materials and methods

2.1. Materials and sample preparation

Dense suspensions were composed using an ASTM C150compliant⁵⁴ ordinary portland cement (OPC) and kaolin clay

[‡] Suspensions in the vicinity of jamming can feature fragility (i.e., particleparticle contact breakage) when the material experiences a rapid change in the direction of applied stress.36,38

Stepper Motor Tail—Nozzle

Tail

Fig. 2 (a) A schematic of the configuration of the 3D-printer consisting of the extruder and cylindrical barrel. All dimensions are expressed in mm. (b) A schematic that illustrates rope coiling of the suspension during extrusion/deposition. The filament with diameter D travels a stand-off distance H from the nozzle tip to the substrate on which it forms a helical coil of radius R_c that rotates with angular frequency ω_c with respect to a vertical axis.

(ACROS Organics)§ at varying kaolin-to-solid (i.e., OPC + clay) volume ratios between 0% and 31%. The upper bound of clay dosage was determined based on: (i) establishing the total solid volume fraction of suspension, that is required to ensure printability, i.e., typically in excess of 0.40, and (ii) the stiffening that results from OPC hydration, which is retarded/suppressed at high clay replacement levels. The median particle diameters (d_{50}) of the OPC and kaolin were 17.2 μ m and 1.4 μ m, respectively, as determined using static light scattering (SLS; LS13-320, Beckman Coulter). The densities of OPC and kaolin were measured as 3140 kg m⁻³ and 2650 kg m⁻³, respectively, using helium pycnometry (Accupyc II 1340, Micromeritics). The suspensions were formed by mixing the powders and water in a 500 mL beaker using a high shear, four-blade impeller-type mixer (RW 20 Digital, IKA) for 180 s at 500 rpm, followed by an additional 180 s of mixing at 600 rpm.

2.2. Printing and fabrication

A layer-wise extrusion system (LUTUM dual v2.0, VormVrij)⁵⁵ fitted with a 5 mm diameter nozzle was used to print the suspensions under controlled air-pressures and flow rates (see Fig. 2a). Following mechanical mixing, the suspension was immediately loaded in a cylindrical barrel ($\approx 600~\rm cm^3$ volume) above the print head and the pressure generated by compressed air was used to force the suspension into a single-screw auger. Different air pressure values ranging between 0.15 MPa and 0.41 MPa were applied to the print cartridge to vary the extrusion velocity of material and the resulting gravitational stress rate that is induced in the print layers/coils (see ESI,† Fig. S1). The nonlinearity between coiling speed and air pressure in Fig. S1 (ESI†) is due to the lubrication layer formation with increasing air pressure that can facilitate material movement in the extruder.

To evaluate the suspension's bucking stability, a rope coiling approach with different coil angular velocities was implemented (see Fig. 2b). A coiling viscous rope features a quasi-vertical tail

that ruptures mainly by gravitational-induced stretching and a helical coil that ruptures primarily by bending. The stand-off distance (i.e., the distance from the nozzle tip to the substrate) was maintained at 50 mm for all suspensions during printing, which enabled the formation of both the tail and coil during printing. During 3D-printing, layers were continuously deposited until failure occurred and the critical height, H_{cr} , corresponding to the buckling instability of the printed coil at failure, was determined. The buckling stability of the coils is primarily controlled by the resistance of the coil to compressive stresses induced by the deposited coils as well as bending resistance of the tail following coiling. 52,53 The total print time was limited to 100 s. It should be noted that the total print time was substantially lower than the time required to form a rigid structure due to OPC hydration (see ESI,† Fig. S2a). The kinetics of structure formation of cementing suspensions can be decomposed in three successive phases: (i) colloidal interaction, (ii) percolated network formation due to the formation of flocs and hydrate nucleation between flocculated particles, followed by (iii) stiffening due to the formation of bonds amongst particles by OPC hydrates. 40,56-58

2.3. Experimental methods

- **2.3.1. Rheological characterization.** The rheology of the suspension was characterized using a combined motor-transducer (CMT) rheometer (Discovery Hybrid Rheometer, DHR-2, TA Instruments) using: (i) vane-in-cup geometry for shear flow/oscillatory rheology, and (ii) parallel plate configuration for extensional rheology. For all measurements, suspensions were conditioned to a temperature of 25 °C \pm 0.1 °C and remained in the dormant hydration period (*i.e.*, when the mixture is still plastic prior to cement hardening)⁵⁹ through the entire time of testing. Four different rheometry protocols were carried out as follows:
- The yield stress σ_y and plastic viscosity η were determined via a shear rate sweep. Before the sweep, a 60 s pre-shear at $\dot{\gamma}=100~{\rm s}^{-1}$ was carried out to remove shear history effects. ⁶⁰⁻⁶² A reversible (ascending-descending) sweep procedure was applied in logarithmically-spaced steps (5 points per decade) from $\dot{\gamma}=0.001~{\rm s}^{-1}$ to 200 s⁻¹ with a 10 s data-averaging period. The apparent yield stress and plastic viscosity were identified as the peak shear stress prior to the suspension's transition to plastic

[§] Certain commercial equipment, software and/or materials are identified in this paper in order to adequately specify the experimental procedure. In no case does such identification imply recommendation or endorsement by the National Institute of Standards and Technology, nor does it imply that the equipment and/or materials used are necessarily the best available for the purpose.

Paper Soft Matter

flow during ascending shear rate sweep^{61,63-65} and the slope of the rising portion of shear stress-shear rate curves ($\dot{\gamma} > 1 \text{ s}^{-1}$), respectively. The ascending sweep (up sweep) was followed by a descending sweep (down sweep) over the same shear rate range. It should be noted that this rheological protocol to characterize stress response of suspension does not reveal the static yield stress when no rest time was allowed between pre-shearing and shear rate sweep (see ESI,† Fig. S2b).66 The rheological protocols used herein are adopted to be relevant for a 3D-printing process wherein no rest time is typically permitted.

- The kinetics of structure formation in the suspensions was characterized via stepwise changes in the shear stress. 67,68 In this method, the shear stress was stepped up between 0 and 200 Pa at 20 Pa increments and held constant for a 30 s period prior to the next step. The shear stress upper bound was selected such that it did not exceed the yield stress of the suspensions ($\sigma_i < \sigma_v$). The pre-shearing regime used was similar to the one used for the shear rate sweep. To mimic the 3D-printing process, no rest time was permitted as shown schematically illustrated in Fig. 1(b).
- The adhesive properties that determine the stretchability of the suspension were characterized via extensional rheology (i.e., tack test).⁶⁹ The sample was placed on the bottom plate and a 1 mm gap was set between the top and bottom plates. A pre-shearing regime similar to that used for the shear rate sweep was used, and no rest time was allowed to suspension. The top plate was raised vertically upward at a controlled velocity of 10 μm s⁻¹ until the sample became separated from the top plate. The normal force experienced by the top plate, corresponding to the stretching force exerted by the suspension, was recorded as a function of the plate's separation distance. The adhesive energy of suspension was then calculated as the area under the force-displacement curve.
- The viscoelastic behavior of the suspension over time was characterized via small amplitude oscillatory shear (SAOS) rheometry. A time sweep (up to 1000 s) was performed at a fixed frequency of 1 Hz and strain amplitude γ = 0.05%. This strain amplitude was selected such that all the suspensions remained in the linear viscoelastic region (LVR).
- 2.3.2. Structure characterization. To assess the floc size of suspensions for varying clay dosages, dynamic light scattering (DLS) analysis (Malvern, Zetasizer Nano) was carried on dilute suspensions (0.05 $g_{\text{solid}}/L_{\text{solution}}$) of OPC-clay solids in aqueous medium of cement pore solution. The Z-average size (intensitybased overall average size) of aggregate was determined by cumulants analysis (Malvern, Zetasizer Software). Optical microscopy (Leica DM750P) was carried out with image capture using a digital camera on similar dilute suspensions as used to assess fractal structuring. Samples used for the optical microscopy were prepared by dripping dilute suspension on the surface of glass slide. To minimize dynamic flow and its subsequent structural changes, the sample was immediately smoothened and squeezed using the edge of another glass slide. Before application, the surfaces of the glass slides were cleaned using isopropanol.
- 2.3.3. Printability and filament homogeneity characterization. To quantify the printability of a suspension following the rope

coiling method, the self-buckling instability was determined when the stack of coils buckled under its own weight upon exceeding a critical height H_{cr} . The gravity-induced stretching of the filament was assessed by determining the maximum stand-off distance (MSOD) at which the extruded filament ruptured under its own weight. To evaluate the potential for liquid phase migration and heterogeneity of materials, the local solid volume fractions were quantified by determining the solid mass of the extrudate by oven drying at 110 $^{\circ}$ C \pm 5 $^{\circ}$ C for 24 h. The measurements were performed on extruded filaments at: (i) different positions of material across the height of the cylindrical barrel, and (ii) different positions across the diameter of the filaments. In (i), at different material displacement in the cylindrical barrel, the air pressure was set at zero to stop extrusion, and then the material remaining in the extruder (around 50 g) was removed and used for the analysis of its solid volume fraction by drying material and determining water content. This procedure was repeated at different positions of material in the cylindrical barrel ($L^* = x/L$, see Fig. 2a). In (ii), extrusion was stopped at $L^* = x/L = 0.5$, and the material remaining in the extruder was extruded to form a filament. The filament $(5 \text{ mm} \times 100 \text{ mm}; D \times H)$ was then sectioned across its diameter to form 3 strips consisting of sections of the following dimensions 1.5 mm \times 100 mm, 2 mm \times 100 mm, and 1.5 mm \times 100 mm. The solid volume fraction of each strip was then determined to evaluate the homogeneity of filament across its diameter.

Results and discussion

3.1. Rheology and fractal structuring of OPC-clay suspensions

The influence of clay dosages on rheology was examined by analysis of the scaling exponents of the measured (apparent) yield stress (see Fig. 3a). Herein, the yield stress-solid volume fraction curves for varying clay dosages were fitted by a power-law function of the form

$$\sigma_{\rm v} = a(\phi)^b,\tag{1}$$

where a and b are fitting variables. Increasing the clay dosage required a lower total solid volume fraction to achieve equivalent yield stress. This reduction arises from strong interparticle interactions and high aspect ratio of the clay particulates, which results in the formation of a house-of-cards structure and a reduction in the interparticle spacing for a given solid content.^{2,70,71} The results of dynamic light scattering (DLS) analysis confirmed that the addition of clay resulted in an increase in floc size (see ESI,† Fig. S3) while producing a structural transition from densely packed flocs in the neat OPC suspension to highly-branched flocs (open structure) in OPC-clay suspension, as evidenced by the optical microscope images (see Fig. 4e and f). The power-law scaling exponent, b, of the yield stress decreased with clay loading (see ESI,† Fig. S4), meaning that the dependence of yield stress on solid volume fraction reduced with clay dosage over a wide range of yield stress-matched suspensions (100 Pa $\leq \sigma_{\rm v} \leq$ 1000 Pa). This results from the formation of fractally-architected aggregates that lead to more uniform arrangements of particles in the

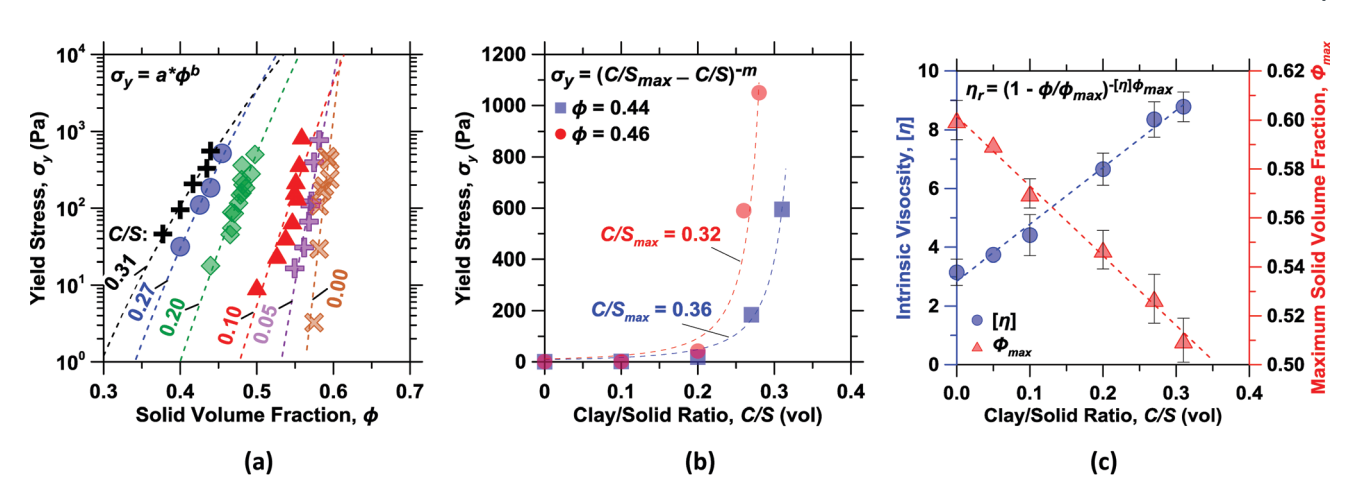


Fig. 3 (a) The yield stress-particle volume fraction curves of dense suspensions for varying clay dosages. The data was fitted by a power-law function of the form $\sigma_v = a(\phi)^b$ to determine the scaling behavior of the yield stress (see ESI,† Fig. S4). (b) The variations in yield stress of suspensions for varying clay dosages as a function of total solid volume fraction. The data was fitted by a power-law function of the form $\sigma_{\rm v} = (C/S_{\rm max} - C/S)^{-m}$ to determine maximum clay dosage C/S_{max} that is achievable for a given total solid volume fraction. (c) The dependence of intrinsic viscosity [η] and maximum solid volume fraction ϕ_{max} on clay dosage. The data was fitted by the Krieger-Dougherty equation (see ESI,† Fig. S4). Here, based on three replicate measurements, a highest uncertainty of 3% in the yield stress and viscosity was observed.

clay-containing suspensions, as indicated by the optical microscopy imaging (see Fig. 4e and f). This behavior is desirable for 3D-printing, since dense suspension can experience shearand/or pressure-induced liquid phase migration during extrusion. Such changes in solid volume fraction - induced due to liquid phase migration (i.e., dewatering of the slurry, locally) can result in the onset of jamming $(\phi \rightarrow \phi_i)$, which causes the cessation of flow in the extruder. At an equivalent total solid volume fraction, the yield stress also exhibited a power-law scaling with clay loading C/S (see Fig. 3b). With increasing total solid volume fraction, ϕ , the yield stress diverges at a lower C/S, indicating that the maximum possible clay loading, C/S_{max} , is dominated by the volume fraction of OPC contained in the suspension. This is on account of the formation of stronger space-spanning networks between clay and OPC particles and reduced interparticle spacing that feature a reduced lubricating liquid film thickness. The electrokinetic interactions in the suspensions were determined using zeta potential data, and calculating the interparticle interaction potential (i.e., the contributions of electrostatic repulsion and van der Waals attraction) between clay particles in DI water and OPC pore solutions (see ESI,† Fig. S5). Cement dissolution produces high ionic strengths (i.e., 0.52 M)⁷² that results in a strong screening of electrostatic repulsions between particles. First, the high ionic strength of OPC pore solutions compresses the electric double layer (EDL) around OPC particles, thereby screening electrostatic repulsions, while increasing the tendency to form aggregates between OPC-OPC particles. Second, only attractive van der Waals forces operate between clay-clay particles in OPC pore solution thus enhancing the potential of their aggregation between clay-clay particles (see ESI,† Fig. S5). Third, the attractive electrostatic interactions between positively charged OPC particles (zeta potential $\zeta = +3.5$ mV) and negatively charged clay particles (zeta potential $\zeta = -0.5$ mV), suggest electrostatically driven heteroaggregate formation.⁷³

In an effort to determine the maximum possible solid fraction or to predict the apparent viscosities of suspensions as a function of particle loading several semi-empirical equations have been proposed. 63 A convenient way to describe viscosity-concentration data is to use the Krieger-Dougherty (K-D) equation.⁷⁴ The K-D equation is written as:⁷⁴

$$\eta_{\rm r} = (1 - \phi/\phi_{\rm max})^{-[\eta]\phi_{\rm max}},$$
(2)

where η_r is the relative viscosity (i.e., ratio of viscosity of the suspension to continuous phase (water)), ϕ_{max} is the maximum solid volume fraction (i.e., cement + clay), and $[\eta]$ is intrinsic viscosity of particles, was fitted to the viscosity-particle volume fraction curves. This equation is not exact, except perhaps in the dilute limit, where it gives the relative viscosity equals 1 plus the intrinsic viscosity times the volume fraction. Therefore, the results obtained for $[\eta]$ and ϕ_{\max} from fitting the K–D equation to the measurements must be seen as displaying trends, and not precisely calculated values. With this proviso, both the values of $[\eta]$ and ϕ_{max} were noted to linearly vary, such that increasing the clay dosage resulted in an increase in $[\eta]$ and conversely, a reduction in ϕ_{max} (see Fig. 3c). The greatest value of ϕ_{max} = 0.60 was obtained for the neat polydisperse OPC suspension (see Fig. 3c), which is surprisingly close to the value of 0.638 noted for random close packing (RCP) of monodisperse hard-spheres.²⁸ This can be used as an indication that the K-D equation is approximate and can only display trends, since even a polydisperse perfect sphere suspension is expected to feature $\phi_{\rm max}$ value much closer to 1 (e.g., $\phi_{\text{max}} = 0.87$ for bimodal system²⁸). The non-sphericity of the cement particles^{75–77} would tend to reduce this value, but it still should be well above the monodisperse sphere results. It should be noted that $[\eta] = 2.5$ for monodisperse hard-spheres, 25,59 and any deviations from the sphere value indicate particle aspect ratio, crowding, and flocculation.^{28,78} For instance, it has been observed that $[\eta]$ varies with particle dispersion state ranging from 5.1 for dispersed suspension

Paper Soft Matter

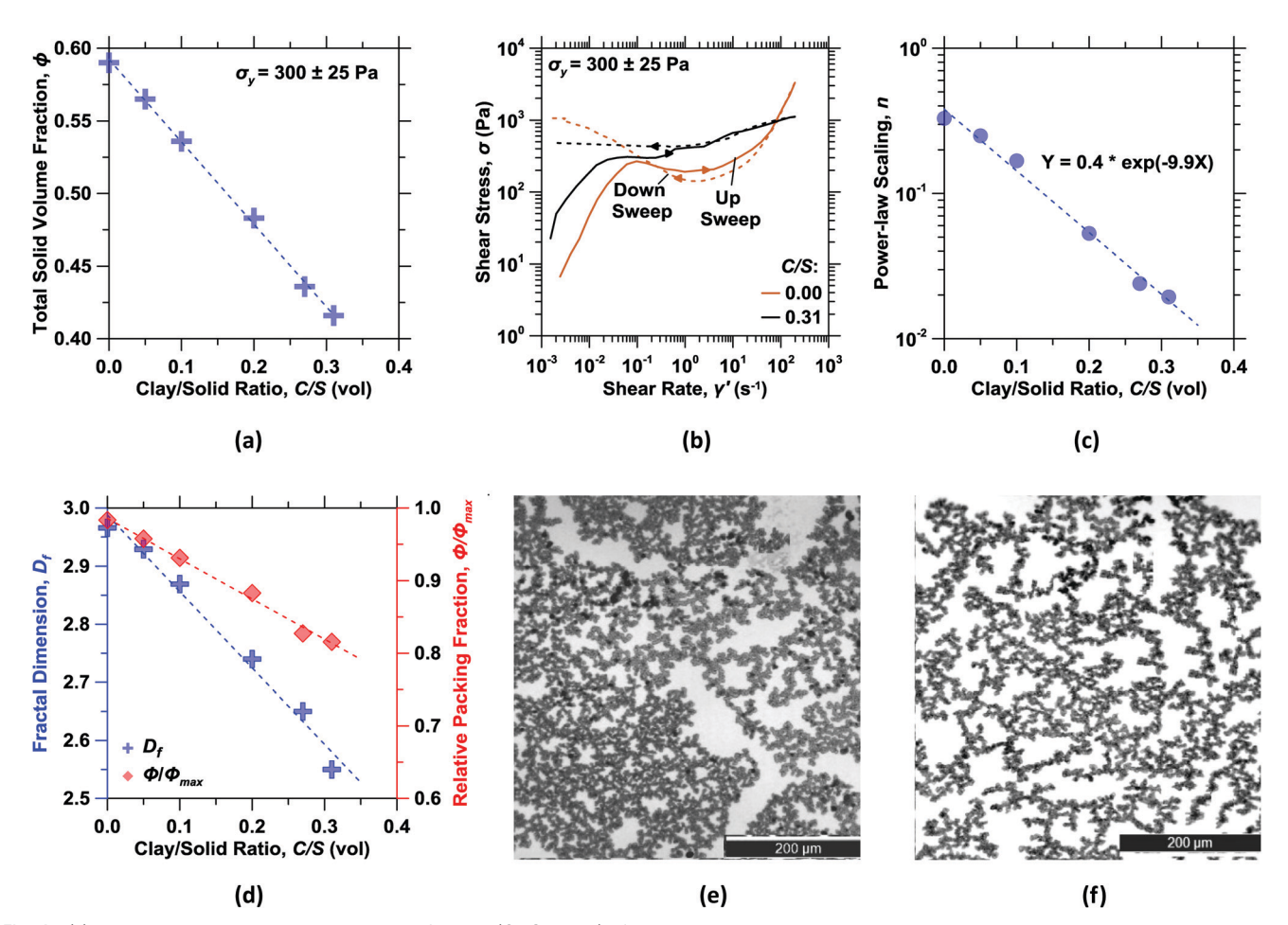


Fig. 4 (a) The variations in the total solid volume fraction (OPC + clay) of the yield stress-matched suspensions in relation to the clay dosage needed to achieve equivalent yield stress; $\sigma_v = 300 \pm 25$ Pa. Here, based on three replicate measurements, the highest uncertainty of 5% in the solid volume fraction was observed. (b) The dependence of shear stress on clay dosage over ascending and descending shear rate sweeps for suspensions with $\sigma_{\rm V}$ = 300 \pm 25 Pa. The scaling of shear stress divergence during the descending shear rate sweep was determined by fitting by a power-law function of the form $\sigma_{\rm v} = a(\gamma')^n$. (c) The dependence of power-law scaling n of shear stress divergence across varying clay dosages. (d) The dependence of the fractal dimension of the solids in the suspensions on clay dosage. The diamond symbols in (d) are marked to the secondary y-axis (i.e., relative packing fraction $\phi/\phi_{\rm max}$) as a function of the clay dosage. Representative optical microscope images that illustrate fractal structuring in (e) the neat OPC suspension and in (f) the clay-enriched suspension (C/S = 31%).

and 6.3 for flocculated suspension.⁷⁹ Since $[\eta]$ is inversely proportional to the skeletal density of clusters, 28 a higher value of $[\eta]$ implies a lower skeletal density of particle agglomerates, suggesting a more open structure as evidenced by increasing floc size with clay addition (see ESI,† Fig. S3). This arises from the dominant interactions between clay-clay particles and their higher particle aspect ratio than OPC particles.

To enable comparison of the structure formation kinetics and the printability of suspensions composed with different clay dosages, their solid volume fractions were adjusted to ensure equivalent yield stress; $\sigma_{\rm v}$ = 300 \pm 25 Pa. On account of increasing interparticle interactions, the solid volume fraction required to match yield stress scaled linearly with clay dosage (see Fig. 4a). Increasing the C/S from 0% to 31% reduced the total solid (i.e., OPC + clay) volume fraction from about 60% for the neat OPC suspension to about 42% for C/S = 31%. This is on account of the fine nature of the clay, and its tendency to adhere water to its surfaces, which demands

dilution to achieve an apparent yield stress equivalent to the clay-free, neat OPC suspension. A closer look at the reversible (ascending-descending) shear rheology curves in Fig. 4b reveals that suspensions composed at equivalent yield stress: $\sigma_{\rm v}$ (300 ± 25 Pa) exhibit a shear stress divergence during both shear-up and shear-down sweeps. This divergence (i.e., nonmonotonic trend) was much more significant for the neat OPC suspension as compared to the clay-enriched suspensions. The shear stress divergence with decreasing shear rate followed a power-law relation of the form

$$\sigma_{\rm r} = a(\gamma')^n \tag{3}$$

where the exponent n decreased from 0.33 for the neat OPC suspension by one order of magnitude with increasing clay dosage (see Fig. 4c). It should be noted that this observation in congruent with rheological hysteresis loop data (see ESI,† Fig. S6), in which the plain OPC suspension exhibited divergence in shear stress during a downward shear rate sweep,

while this behavior was substantially suppressed for the OPCclay suspension. Furthermore, on account of higher thixotropic structure rebuilding, the OPC-clay suspension featured a greater hysteresis loop area than that of the plain OPC suspension. 48,80

The divergence of the shear stress curves observed in Fig. 4(b) for the neat OPC suspension can be attributed to shear-induced structural inhomogeneities that produce mechanically unstable behavior. When particles are forced into close proximity at high shear rates, the lubricating water film thickness is reduced, leading to the formation of frictional contacts between particles. This can result in solid-like behavior of suspensions when the shear rate increases, indicating discontinuous shear thickening, as identified by the jump in viscosity-shear rate trend (see ESI,† Fig. S7). When the applied shear stress was reversed (downward shear sweep), the neat OPC suspension experienced nonmonotonic behavior. However, this non-monotonic response was found to diminish with increasing clay dosage (see Fig. 4c). More stable behavior in OPC-clay suspensions can be attributed to the (i) stronger interparticle interactions between clayclay and clay-OPC particles, (ii) the lower total solid volume fraction in suspension (lower relative volume fraction $\phi/\phi_{\rm max}$) that is required to achieve an equivalent yield stress to that of the neat OPC suspension, and (iii) fractal structuring transition from densely packed flocs to highly branched flocs (i.e., space-spanning network) in the OPC-clay suspensions that can hinder local liquid phase migration amongst particles. To assess the structure of aggregates within the OPC-clay suspensions, their fractal dimensions were determined assuming strong gels, in which the interfloc links are as strong as the intrafloc linkages:81

$$b = (d' + X)/(d' - D_{\rm f}), \tag{4}$$

where *b* is the power-law scaling from the yield stress–particle volume fraction curves (see Fig. 3a and ESI,† Fig. S4), D_f is the fractal dimension of the aggregate cluster, d' is the Euclidean dimension (d' = 3), and X is the bond dimension that describes

the fractal geometry of the cluster backbone ($X \approx 1.0^{81,82}$). A value of $D_{\rm f} \approx 3$ was determined for the neat OPC suspension with $\phi/\phi_{\rm max} \approx 1$ indicating no fractal behavior wherein particles aggregate into closely-packed assemblages. Conversely, the fractal dimension decreased with clay addition, wherein the aggregates tend to form fractally-architected regions that feature a more open structure, thereby resulting in more uniform arrangements of particles, as evidenced by optical microscopy (see Fig. 4e and f).

3.2. Structure formation kinetics of OPC-clay suspensions

The kinetics of structure formation and the deformation resistance of the suspensions were thereafter probed using the stepped-isostress method (see Fig. 5a). Within each step, the suspension experienced an instantaneous strain that was followed by transient strain, which reached a plateau. In general, the extent of instantaneous strain and the rate of transient strain were strongly reduced by clay dosage. To determine the time required to reach a plateau for each cycle, i.e., the relaxation time, a Kelvin-Voigt model of the form⁸³

$$\gamma_t = \sum_{i=1}^{N=10} A_i \left(1 - e^{-\frac{t}{I_{r,i}}} \right), \tag{5}$$

was fitted to the data, where $t_{\rm r,i}$ is the retardation time (*i.e.*, relaxation time) and A_i is a fitting parameter. This approach is analogous to creep flow characterization using the Boltzmann superposition principle (i.e., time-aging-stress) of soft glassy materials that show strong time and stress dependency.84,85 Semi-log plots showing γ - t_r collapses all cycles on a single master curve for each suspension (see Fig. 5b). It should be noted that although the retardation times were extracted by fitting eqn (5) to each shear stress cycle of 30 s, in effect, some strain trends did not truly reach a plateau, specially at higher shear stress cycles, as indicated in the zoomed view (see ESI,† Fig. S8). Herein, it is seen that structural rebuilding that is induced by the clay particles results in a lower deformation rate as indicated by a greater

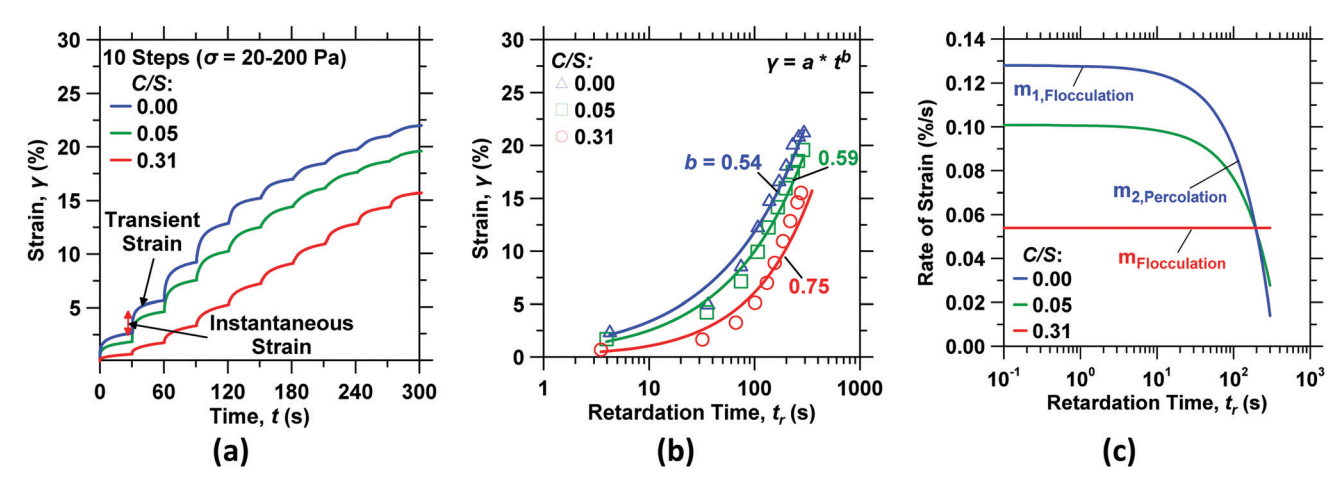


Fig. 5 (a) The evolution of strain with stepwise changes in shear stress for varying clay dosages. The shear stress was stepped up between 0 and 200 Pa at 20 Pa increments over 10 steps and held constant for a 30 s period prior to next step over a cumulative period of 300 s. (b) The master curves of strain responses using data shown in (a) that are obtained by fitting to the Kelvin-Voigt model. (c) The dependence of strain rate on clay dosage. The deviation from the initial slope captures the transition from flocculation to percolation (i.e., short-term stiffening) in the suspension.

Paper Soft Matter

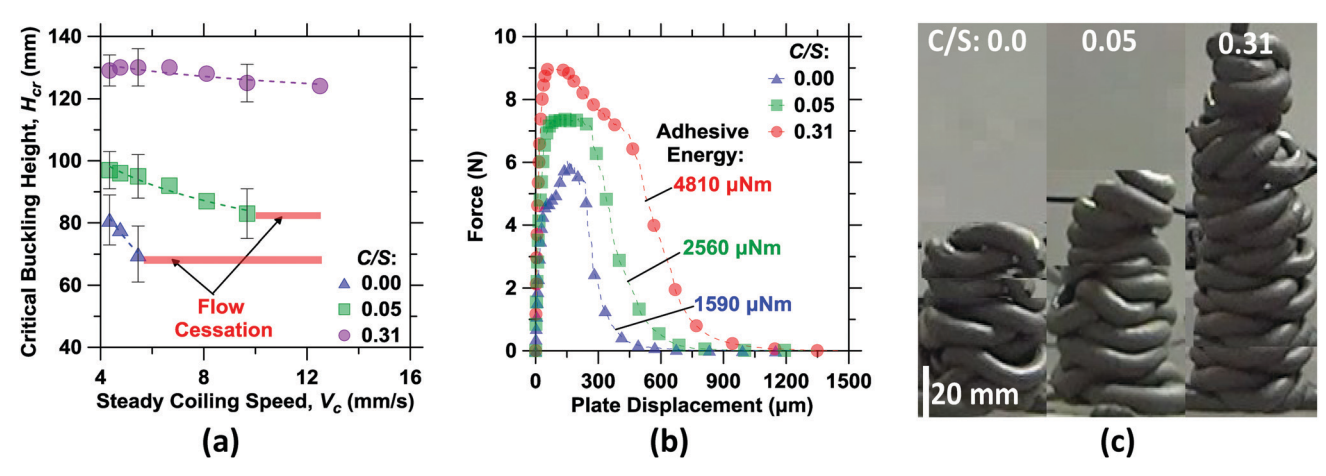


Fig. 6 (a) The dependence of critical buckling height on clay dosage across different coiling speeds. The red zone represents coiling speeds beyond which the flow of suspensions was arrested in the extruder. Based on three replicate measurements, the highest uncertainty of 9% in the critical buckling height was observed. (b) Representative normal force-plate displacement responses for suspensions subjected to extensional rheology across clay dosages. The adhesive energy of suspension was calculated as the area under the force-plate displacement curve. (c) The critical buckling heights corresponding to the onset of buckling instability. Unlike clay-enriched suspensions, the neat OPC suspension featured rapid filament rupture during deposition.

power-law scaling b for clay-enriched suspensions. The rate of strain development is controlled by: (i) thixotropic rebuilding that is dominated by flocculation, and (ii) short-term stiffening that is induced by the formation of a percolated network at pseudocontact points.¶ 40,86 The formation of a percolated network is suggested to be caused by both physical and chemical changes. 58,86 The physical effect is linked to the time-dependent colloidal flocculation, which tends to bring particles into contacts while the chemical effect results from formation of percolated network between particles via nucleation and growth of hydrates at pseudo-contact points between flocculated particles. 40

Closer analysis of the kinetics of structure formation of OPC-clay suspensions indicates that the suspensions demonstrate transition points with initial slope m_1 corresponding to flocculation with a progressive switchover, with time, to percolation slope m_2 (see Fig. 5c). The contribution of flocculation to the strain rate remains constant as indicated by a constant slope m_1 in Fig. 5c. However, due to the progressive formation of percolated networks between particles, the contribution of short-term kinetics to reducing the strain rate increases progressively (see Fig. 5c). As such, the contributions of flocculation and percolation due to the short-term kinetics of suspension structure formation to deformation associated with deposition of subsequent overlying layers can be estimated by an equation of the form

$$\frac{\mathrm{d}\gamma}{\mathrm{d}t} = m_{1,\text{for } t < t_c} + \exp(m_2 \cdot t)_{\text{for } t > t_c} \tag{6}$$

where m_1 is the flocculation rate, which is constant up to the onset of percolated network formation, and m_2 (t_c ,t) is the percolation rate, which initiates at time t_c (*i.e.*, transition from

flocculation to percolation) and varies exponentially with time. Notably, as a result of OPC dilution, clay dosages delay stiffening. For example, the 31% clay suspension exhibited solely the earlyage slope m_1 , suggesting that the contribution of short-term stiffening is minimal. These observations are in agreement with the non-linear structural build-up of storage modulus (see ESI,† Fig. S9b). The initial storage modulus is related to the degree of flocculation while the evolution rate of storage modulus is controlled by percolated network formation.

3.3. Buckling stability and filament homogeneity of OPC-clay suspensions

The resistance to buckling, *i.e.*, the buckling stability of the filament is controlled by both the structure formation kinetics and filament homogeneity. The former is important to sustain stability during layer build-up while the latter ensures consistent properties of the filament during deposition to minimize imperfections during printing. The critical buckling height, $H_{\rm cr}$, of the suspensions was noted to enhance significantly with clay dosage across coiling speeds (see Fig. 6a). This enhancement is attributed to both the (i) improved structural recovery following deposition, which reduces deformations of the deposited filament as indicated by its faster flocculation (see Fig. 5), and (ii) greater stretchability, which limits the potential for filament rupture when subjected to stretching (tail portion) and bending (coil portion).

The buckling stability of coiling of an elastic rope has been found to scale with the gravitational-bending length $L_{\rm gb}$, which is driven the balance between bending and gravitational energies:

$$L_{\rm gb} = \left(Er_0/8\rho g\right)^{1/3} \tag{7}$$

where E is the material Young's modulus, r_0 is the radius of the filament, and ρ is the material density.⁸⁷ As such, materials with a higher zero-shear rate storage modulus G' are expected

[¶] Pseudo-contact points refer to connectivity between particles in cementing suspensions that are connected by colloidal interactions rather than by cement hydration products, which, all together, results in formation of percolated networks between particles.

to have greater buckling stability. In addition to the elastic property, stretchability is another important factor controlling the stability of suspension following coiling. To quantitatively assess the stretchability, the adhesive properties (i.e., cohesion and adhesion)⁸⁸ of the suspensions were determined using extensional rheology (see Fig. 6b). The greater force peak and slower force decay indicate greater cohesion of the clayenriched suspensions. This also results in greater adhesive energy in clay-enriched suspensions as evidenced by the larger area under the load-displacement curve obtained from extensional rheology. Unlike OPC-clay suspensions, the neat OPC suspension exhibited a strain-hardening response. It should be noted that both plain OPC and OPC-clay suspensions were drawn towards the center of the plate and no fingering instability was observed for the OPC-clay suspensions during extensional rheology. The strain hardening behavior for the plain OPC suspension is expected to be due to its high solid volume fraction, which can result in a higher interparticle friction and interlocking when suspension moves towards the center of the plate.88 Increasing frictional contacts between particles induce an enhanced tendency to rupture as evidenced by the sharp force decay following the peak force.

Coming back to buckling, it is notable that the 31% clay suspension showed essentially an unchanged critical buckling height across coiling speeds. This suggests that the structural recovery of these suspensions was fast enough to sustain the increased loading rate. On the other hand, the buckling stability of the neat OPC suspension (and suspensions composed of lower clay dosages) diminished significantly with coiling speed, suggesting that the rate of structural recovery was inferior to the coiling speed and the loading rate imposed therein. In addition to retarded structural recovery, the neat OPC suspension featured filament fragility (i.e., rupture and discontinuity) following extrusion and deposition due to its low

stretching and bending capacities (see Fig. 6c). Such filament rupture creates imperfections that accelerate buckling instability and yielding. As a result, the printed coils consisting of the neat OPC suspension dominantly fail by material yielding. However, the clay-containing suspensions fail dominantly due to a buckling instability since the accelerated structural recovery and enhanced stretchability offered by clay particulates enhances both the normal and bending capacities of the filament, thus enhancing its resistance to yielding.

To better assess the stretchability of the filament, the maximum stand-off distance (MSOD) at which a filament can withstand its own weight was measured (see Fig. 7a). It was noted that the MSOD scaled linearly with the adhesive energy of the suspension, indicating that - expectedly - a more "sticky" suspension features better filament continuity. Importantly, a sequence of images obtained from video recording of crack propagation and rupture mode revealed that the neat OPC suspension exhibited elastic rupture wherein a crack initiated at the edge and propagated inward (i.e., edge fracture) while the clay-enriched suspension featured necking failure (i.e., ductile failure) – more similar to plasticity-driven failure. This suggests that in the neat OPC suspension, strain localization, caused by local dewatering along the filament's length/diameter, formed fracture critical regions during extrusion and deposition. Indeed, more detailed analyses of local particle density variations of the filament as a function of both relative position of material in the cylindrical barrel and along the filament diameter indicated that the neat OPC suspension underwent significant changes in particle volume fraction during 3D-printing/ extrusion; unlike the clay-enriched suspensions (see Fig. 7b and c). This was qualitatively suggested by visual evidence of water leakage from the extruder indicative of the dewatering of the OPC suspension. It has been observed that the imposition of extrusion pressure and shear can lead to the formation of

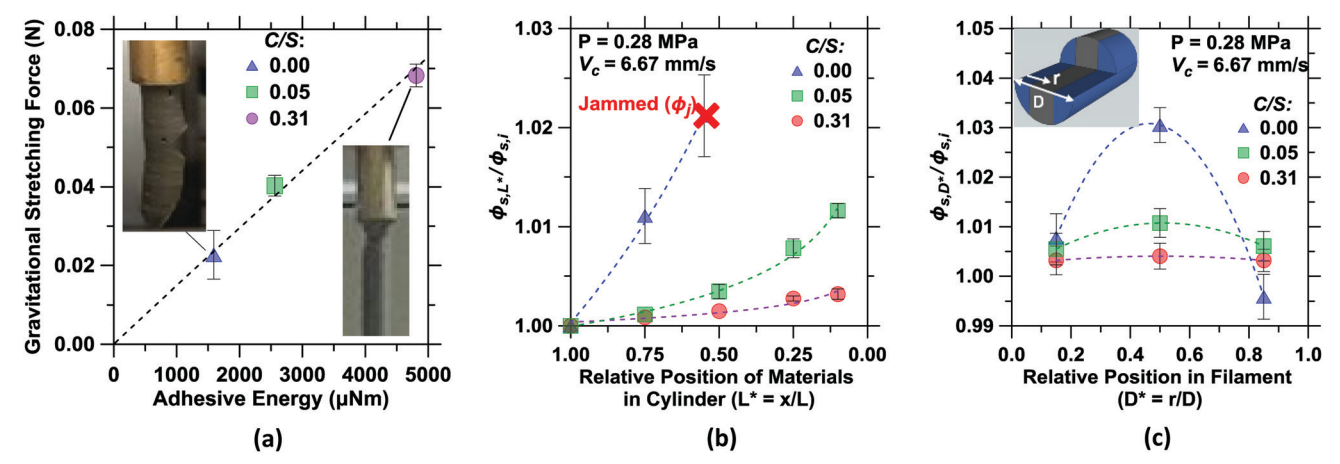


Fig. 7 (a) The correlation between adhesive energy of the suspension and maximum stand-off distance of its filament. The maximum stand-off distance (MSOD) was determined as the allowable filament length that was able to support its weight when subjected to gravity-induced stretching. The insets compare the rupture modes of the OPC and clay-enriched suspensions subjected to gravity-induced stretching. (b) The variation in the relative solid volume fraction of the filament as a function of the relative length of material in the cylindrical barrel during extrusion. (c) The variation in the relative solid volume fraction of filament as a function of its relative diameter during extrusion. The inset illustrates the defined relative position across filament diameter. Based on three replicate measurements, a maximum 3% deviation in solid volume fraction was observed.

different zones, including plug flow, shearing, and dead regions, within the material in the extruder. 10,11 This can induce liquid phase migration, which may result either in flow cessation due to a reduced lubricating water film thickness or the formation of solid-poor regions in the filament. 6,10 This results in heterogeneous gradients of particle volume fraction in the filament (see Fig. 7c). This behavior is critical for suspensions whose particle volume fraction is in the vicinity of the jamming volume fraction ϕ_i , where a small local increase in solid concentration associated with liquid phase migration can cause cessation of flow and bring the suspension to the jammed state, $\phi \rightarrow \phi_i$, in the extruder.89 This is indicated by the sharp power-law scaling of yield stress with ϕ for the neat OPC suspension (see ESI,† Fig. S4) wherein the yield stress rapidly increases with a small increase in solid concentration. On the other hand, minimal changes in particle volume fraction induced by shear are noted in the clayenriched suspension, since their lower relative volume fraction $\phi/\phi_{\rm max}$ and the fractally-architected arrangement of aggregates arrests water within flocs and consequently reduces liquid phase migration (see Fig. 7b and c). Thus, reducing the dewatering of the suspension is a critical need to ensure ease and consistency of extrusion during the 3D-printing process.

4. Summary and conclusions

This paper has elucidated the influences of clay particulates on controlling fractal structuring and flow cessation in extruder and homogeneity of cementing suspensions in the context of the 3D-printing process. Special focus was placed on understanding how the rope-coiling method can be used to assess the buckling stability and fragility of the extruded filament - during 3D-printing - for suspensions loaded with clay additives. In general, it is noted that neat OPC suspensions feature a steep stress-shear rate relationship, resulting from their closely-packed structure with $\phi \approx \phi_{\rm max}$ and fractal dimension $D_{\rm f} \approx 3$. The dosage of clay particulates is found to decrease the power-law divergence (i.e., non-monotonic behavior) of shear stress and mitigate flow cessation in the extruder. This is linked to the (i) stronger interparticle interactions between clay/OPC particles, (ii) decreased relative packing fraction (ϕ/ϕ_{max}) , and (iii) the formation of fractally-architected aggregates in the OPC-clay suspensions which can suppress the mechanically unstable behavior in shear stress response. Alterations in fractal structuring of aggregates from densely packed flocs in the neat OPC suspension to highly-branched flocs (i.e., spacespanning network) in the OPC-clay suspension results in more uniform particle arrangements that can increase the resistance to liquid-phase migration (i.e., slurry dewatering) when shear stress is applied. The analysis of interparticle interactions indicates that high ionic strengths resulting from cement dissolution disrupt electrostatic repulsion between clay-clay particles by screening charges, thus resulting in a significant interparticle interactions between all particles (clay-clay, OPCclay, and OPC-OPC particles) in the OPC-clay suspensions. Importantly, the clay-enriched suspensions due to their greater

structural recovery rate and stretchability feature higher critical buckling heights across varying coiling speeds than the neat OPC suspension. The ability of clay additions to prevent dewatering is critical for dense suspensions whose particle volume fraction is in the vicinity of the jamming volume fraction ϕ_i . Since dewatering causes the solid volume fraction to approach $\phi \rightarrow \phi_i$, which results in flow cessation in the extruder, maintaining $\phi < \phi_{\rm i} \approx \phi_{\rm max}$ is a key factor for ensuring the printability of dense suspensions. The understanding gained herein offers new means to design, evaluate, and rank dense suspensions to ensure superior filament homogeneity (i.e., hindering dewatering) and stretchability. These attributes are of relevance to slurry-based 3D-printing processes wherein the filament undergoes substantial stretching and bending actions due to changes in the stand-off distance or print path curvature.

Conflicts of interest

There are no conflicts to declare.

Acknowledgements

The authors acknowledge financial support for this research from: the Anthony and Jeanne Pritzker Family Foundation, TRANSCEND: a joint UCLA-NIST consortium that is supported by its industry and agency partners, and the National Science Foundation (DMREF: 1922167). This research was conducted in the Laboratory for the Chemistry of Construction Materials (LC²). As such, the authors gratefully acknowledge the support that has made these laboratories and their operations possible. The contents of this paper reflect the views and opinions of the authors, who are responsible for the accuracy of the datasets presented herein, and do not reflect the views and/or policies of the funding agencies, nor do the contents constitute a specification, standard or regulation.

References

- 1 F. Gadala-Maria and A. Acrivos, J. Rheol., 1980, 24, 799-814.
- 2 J. A. Lewis, J. Am. Ceram. Soc., 2000, 83, 2341-2359.
- 3 A. Gahler, J. G. Heinrich and J. Guenster, J. Am. Ceram. Soc., 2006, 89, 3076-3080.
- 4 X. Tian, D. Li and J. G. Heinrich, Rapid prototyping journal, 2012, 18, 362-373.
- 5 J. Cesarano, MRS Online Proceedings Library Archive.
- 6 A. Perrot, D. Rangeard, Y. Mélinge, P. Estellé and C. Lanos, Appl. Rheol., 2009, 19, 53042.
- 7 A. Perrot, D. Rangeard and A. Pierre, Mater. Struct., 2016, 49,
- 8 T. Wangler, E. Lloret, L. Reiter, N. Hack, F. Gramazio, M. Kohler, M. Bernhard, B. Dillenburger, J. Buchli and N. Roussel, RILEM Technical Lett., 2016, 1, 67-75.
- 9 S. A. Nair, H. Alghamdi, A. Arora, I. Mehdipour, G. Sant and N. Neithalath, J. Am. Ceram. Soc., 2019, 102, 3951-3964.

- 10 Z. Toutou, N. Roussel and C. Lanos, Cem. Concr. Res., 2005, 35, 1891–1899.
- 11 H. Khelifi, A. Perrot, T. Lecompte, D. Rangeard and G. Ausias, *Powder Technol.*, 2013, **249**, 258–268.
- 12 N. Roussel, Cem. Concr. Res., 2018, 112, 76-85.

- 13 L. Reiter, T. Wangler, N. Roussel and R. J. Flatt, *Cement and Concrete Research*, 2018, **112**, 86–95.
- 14 A. R. Torrado, C. M. Shemelya, J. D. English, Y. Lin, R. B. Wicker and D. A. Roberson, *Additive Manufacturing*, 2015, 6, 16–29.
- 15 R. J. M. Wolfs, F. P. Bos and T. A. M. Salet, *Cem. Concr. Res.*, 2018, **106**, 103–116.
- 16 A. S. J. Suiker, Int. J. Mech. Sci., 2018, 137, 145-170.
- 17 G. Ovarlez, L. Tocquer, F. Bertrand and P. Coussot, *Soft Matter*, 2013, 9, 5540–5549.
- 18 N. Koumakis, E. Moghimi, R. Besseling, W. C. Poon, J. F. Brady and G. Petekidis, *Soft Matter*, 2015, **11**, 4640–4648.
- 19 G. Colombo, S. Kim, T. Schweizer, B. Schroyen, C. Clasen, J. Mewis and J. Vermant, J. Rheol., 2017, 61, 1035–1048.
- 20 R. J. M. Wolfs, F. P. Bos and T. A. M. Salet, Cem. Concr. Compos., 2019, 103344.
- 21 T. Wang and B. Derby, J. Am. Ceram. Soc., 2005, 88, 2053-2058.
- 22 M. Schwentenwein and J. Homa, *Int. J. Appl. Ceram. Technol.*, 2015, 12, 1–7.
- 23 A. J. Liu and S. R. Nagel, Nature, 1998, 396, 21.
- 24 V. Trappe, V. Prasad, L. Cipelletti, P. N. Segre and D. A. Weitz, *Nature*, 2001, 411, 772.
- 25 E. Brown, N. A. Forman, C. S. Orellana, H. Zhang, B. W. Maynor, D. E. Betts, J. M. DeSimone and H. M. Jaeger, *Nat. Mater.*, 2010, 9, 220.
- 26 R. Mari, R. Seto, J. F. Morris and M. M. Denn, J. Rheol., 2014, 58, 1693–1724.
- 27 N. J. Wagner and J. F. Brady, Phys. Today, 2009, 62, 27-32.
- 28 J. Mewis and N. J. Wagner, *Colloidal suspension rheology*, Cambridge University Press, 2012.
- 29 W. Yang, Y. Wu, X. Pei, F. Zhou and Q. Xue, *Langmuir*, 2017, 33, 1037–1042.
- 30 N. M. James, E. Han, R. A. L. de la Cruz, J. Jureller and H. M. Jaeger, *Nat. Mater.*, 2018, 17, 965.
- 31 E. Brown, N. A. Forman, C. S. Orellana, H. Zhang, B. W. Maynor, D. E. Betts, J. M. DeSimone and H. M. Jaeger, *Nat. Mater.*, 2010, **9**, 220.
- 32 N. M. James, H. Xue, M. Goyal and H. M. Jaeger, *Soft matter*, 2019, **15**, 3649–3654.
- 33 J. F. Morris, Phys. Rev. Fluids, 2018, 3, 110508.
- 34 N. Fernandez, R. Mani, D. Rinaldi, D. Kadau, M. Mosquet, H. Lombois-Burger, J. Cayer-Barrioz, H. J. Herrmann, N. D. Spencer and L. Isa, *Phys. Rev. Lett.*, 2013, **111**, 108301.
- 35 A. J. Liu and S. R. Nagel, *Annu. Rev. Condens. Matter Phys.*, 2010, 1, 347–369.
- 36 R. Seto, A. Singh, B. Chakraborty, M. M. Denn and J. F. Morris, *Granular Matter*, 2019, 21, 82.
- 37 M. Gameiro, A. Singh, L. Kondic, K. Mischaikow and J. F. Morris, *Phys. Rev. Fluids*, 2020, 5, 034307.
- 38 M. E. Cates, J. P. Wittmer, J.-P. Bouchaud and P. Claudin, *Phys. Rev. Lett.*, 1998, **81**, 1841.

- 39 S. D. Kulkarni, B. Metzger and J. F. Morris, *Phys. Rev. E: Stat., Nonlinear, Soft Matter Phys.*, 2010, **82**, 010402.
- 40 N. Roussel, G. Ovarlez, S. Garrault and C. Brumaud, *Cem. Concr. Res.*, 2012, **42**, 148–157.
- 41 H. van Olphen, An Introduction to Clay Colloid Chemistry: For Clay Technologists, Geologists, and Soil Scientists, 1977.
- 42 B. Rand and I. E. Melton, *J. Colloid Interface Sci.*, 1977, **60**, 308–320.
- 43 E. Paineau, L. J. Michot, I. Bihannic and C. Baravian, *Langmuir*, 2011, 27, 7806–7819.
- 44 U. Brandenburg and G. Lagaly, *Appl. Clay Sci.*, 1988, 3, 263–279.
- 45 G. Lagaly, Appl. Clay Sci., 1989, 4, 105-123.
- 46 P. F. Luckham and S. Rossi, *Adv. Colloid Interface Sci.*, 1999, **82**, 43–92.
- 47 M. J. Solomon, A. S. Almusallam, K. F. Seefeldt, A. Somwangthanaroj and P. Varadan, *Macromolecules*, 2001, 34, 1864–1872.
- 48 J. Mewis and N. J. Wagner, *Adv. Colloid Interface Sci.*, 2009, 147, 214–227.
- 49 F. A. Andrade, H. A. Al-Qureshi and D. Hotza, *Appl. Clay Sci.*, 2011, **51**, 1–7.
- 50 D. P. Bentz, J. M. Davis, M. A. Peltz and K. A. Snyder, *Mater. Struct.*, 2014, 47, 581–589.
- 51 E. Keita, H. Bessaies-Bey, W. Zuo, P. Belin and N. Roussel, Cem. Concr. Res., 2019, 123, 105787.
- 52 N. M. Ribe, M. Habibi and D. Bonn, *Phys. Fluids*, 2006, **18**, 084102.
- 53 M. Habibi, N. M. Ribe and D. Bonn, *Phys. Rev. Lett.*, 2007, 99, 154302.
- 54 ASTM C150/C150M 18: Standard Specification for Portland Cement, ASTM International, West Conshohocken, PA, 2018.
- 55 VormVrij, (n.d.). http://lutum.vormvrij.nl/.
- 56 P. F. G. Banfill, in Proceedings of the 11th international cement chemistry congress, 2003, vol. 1, pp. 50–62.
- 57 N. Roussel, Cem. Concr. Res., 2005, 35, 1656-1664.
- 58 A. M. Mostafa and A. Yahia, Cem. Concr. Res., 2016, 85, 174–182.
- 59 H. F. Taylor, Cement chemistry, Thomas Telford, 1997.
- 60 S. A. Nair, H. Alghamdi, A. Arora, I. Mehdipour, G. Sant and N. Neithalath, *J. Am. Ceram. Soc.*, 2019, **102**, 3951–3964.
- 61 K. Vance, G. Sant and N. Neithalath, *Cem. Concr. Compos.*, 2015, **59**, 38–48.
- 62 F. Khalkhal, P. J. Carreau and G. Ausias, *J. Rheol.*, 2011, 55, 153–175.
- 63 J. Mewis and N. J. Wagner, Colloidal suspension rheology, Cambridge University Press, 2012.
- 64 Q. D. Nguyen and D. V. Boger, Annu. Rev. Fluid Mech., 1992, 24, 47–88.
- 65 P. R. de Souza Mendes and R. L. Thompson, *Rheol. Acta*, 2013, 52, 673–694.
- 66 D. Bonn, M. M. Denn, L. Berthier, T. Divoux and S. Manneville, *Rev. Mod. Phys.*, 2017, 89, 035005.
- 67 T. A. Tervoort, E. T. J. Klompen and L. E. Govaert, *J. Rheol.*, 1996, 40, 779–797.

Paper

68 S. Jazouli, W. Luo, F. Brémand and T. Vu-Khanh, *J. Mater. Sci.*, 2006, 41, 531–536.

- 69 D. Derks, A. Lindner, C. Creton and D. Bonn, *J. Appl. Phys.*, 2003, **93**, 1557–1566.
- 70 V. Gupta, M. A. Hampton, J. R. Stokes, A. V. Nguyen and J. D. Miller, *J. Colloid Interface Sci.*, 2011, 359, 95–103.
- 71 Y. H. Lee, C. B. Park, M. Sain, M. Kontopoulou and W. Zheng, *J. Appl. Polym. Sci.*, 2007, **105**, 1993–1999.
- 72 J. N. Israelachvili, *Intermolecular and surface forces*, Academic Press, 2015.
- 73 A. Y. Kim and J. C. Berg, J. Colloid Interface Sci., 2000, 229, 607–614.
- 74 I. M. Krieger and T. J. Dougherty, *Trans. Soc. Rheol.*, 1959, 3, 137–152.
- 75 E. J. Garboczi and J. W. Bullard, *Cem. Concr. Res.*, 2004, 34, 1933–1937.
- 76 S. T. Erdoğan, X. Nie, P. E. Stutzman and E. J. Garboczi, *Cem. Concr. Res.*, 2010, 40, 731–739.
- 77 L. Holzer, R. J. Flatt, S. T. Erdoğan, J. W. Bullard and E. J. Garboczi, *J. Am. Ceram. Soc.*, 2010, **93**, 1626–1633.
- 78 D. B. Genovese, Adv. Colloid Interface Sci., 2012, 171, 1-16.

- 79 L. Struble and G.-K. Sun, Adv. Cem. Based Mater., 1995, 2, 62-69.
- 80 T. Divoux, V. Grenard and S. Manneville, *Phys. Rev. Lett.*, 2013, **110**, 018304.
- 81 W.-H. Shih, W. Y. Shih, S.-I. Kim, J. Liu and I. A. Aksay, *Phys. Rev. A: At., Mol., Opt. Phys.*, 1990, 42, 4772.
- 82 J. P. Pantina and E. M. Furst, *Phys. Rev. Lett.*, 2005, **94**, 138301.
- 83 F. Mainardi and G. Spada, Eur. Phys. J.: Spec. Top., 2011, 193, 133–160.
- 84 M. Cloitre, R. Borrega and L. Leibler, *Phys. Rev. Lett.*, 2000, 85, 4819.
- 85 A. Shukla and Y. M. Joshi, Rheol. Acta, 2017, 56, 927-940.
- 86 W.-G. Lei and L. J. Struble, J. Am. Ceram. Soc., 1997, 80, 2021–2028.
- 87 M. K. Jawed, F. Da, J. Joo, E. Grinspun and P. M. Reis, *Proc. Natl. Acad. Sci. U. S. A.*, 2014, **111**, 14663–14668.
- 88 A. Kaci, R. Bouras, V. T. Phan, P. A. Andréani, M. Chaouche and H. Brossas, *Cem. Concr. Compos.*, 2011, 33, 218–224.
- 89 R. Besseling, L. Isa, P. Ballesta, G. Petekidis, M. E. Cates and W. C. K. Poon, *Phys. Rev. Lett.*, 2010, **105**, 268301.